# Chapter 18

# Surface Deformation of Augustine Volcano, 1992–2005, from Multiple-Interferogram Processing Using a Refined Small Baseline Subset (SBAS) Interferometric Synthetic Aperture Radar (InSAR) Approach

By Chang-Wook Lee[1], Zhong Lu[2], Hyung-Sup Jung[3], Joong-Sun Won[4], and Daniel Dzurisin[5]

## Abstract

Augustine Volcano is an active stratovolcano located in southwestern Cook Inlet, about 280 kilometers southwest of Anchorage, Alaska. The volcano produced six significant explosive eruptions between 1812 and 1986. Augustine eruptions typically have an explosive onset followed by dome building. The most recent eruption began on January 11, 2006. We applied the small baseline subset (SBAS) interferometric synthetic aperture radar (InSAR) technique to measure ground surface deformation during 1992–2005 with the use of European Remote Sensing Satellites 1 and 2 (ERS–1 and ERS–2) radar imagery. Through a multiple-interferogram approach, atmospheric delay artifacts, which hinder conventional InSAR measurements, are significantly reduced by spatial and temporal filtering. This allows us to retrieve time-series deformation over coherent points at millimeter-scale accuracy. The deformation results from two independent satellite tracks agree with each other, suggesting 2 to 8 cm wholesale uplift of Augustine Volcano from 1992 to 2005. Global Positioning System (GPS) data acquired in September 2004 and October 2005 confirm the SBAS InSAR results. A preliminary model consisting of a contracting source at 2 to 4 km depth and an inflating source at 7 to 12 km depth fits the observed deformation reasonably well. We interpret the deeper source as a long-term magma storage zone and the shallower source as a subsidiary reservoir that was tapped during the 2006 eruption. The shallow source corresponds approximately to the location of the volcano-tectonic earthquakes that preceded and followed the 1976 and 2006 eruptions, respectively.

## Introduction

Mapping volcanic deformation between eruptions can provide important clues to the magma plumbing system and magma supply rate (Dzurisin, 2007). Ground-based techniques, including Global Positioning System (GPS) observations, leveling, and tiltmeters, can measure subtle deformation with an accuracy of a few millimeters. Even though these ground-based techniques can provide accurate point-to-point deformation measurements, they are relatively expensive, logistically challenging, and often inadequate to characterize complex deformation patterns that sometimes are associated with eruptions (Dzurisin, 2007). Interferometric synthetic aperture radar (InSAR) is a satellite-based technique for mapping large-area surface deformation. InSAR has become an important tool for studying volcanoes in Alaska (Lu and others, 2007) and around the world (Zebker and others, 2000). In theory, InSAR can measure relative surface displacements with an accuracy of a few millimeters (Gabriel and others, 1989). In reality, however, atmospheric delay noise and other

[1]ASRC Research and Technology Solutions, contractor to USGS, 1300 SE Cardinal Court, Vancouver, WA 98683.

[2]U.S. Geological Survey, EROS Center and Cascades Volcano Observatory, 1300 SE Cardinal Court, Vancouver, WA 98683-9589.

[3]Department of Geoinfomatics, The University of Seoul, 90 Jeonnong-dong, Dongdaemun-gu, Seoul 130-743, Korea.

[4]Department of Earth System Sciences, Yonsei University, 134 Shinchon-dong, Seodaemun-gu, Seoul, 120-749, Korea.

[5]U.S. Geological Survey, Cascades Volcano Observatory, 1300 SE Cardinal Court, Vancouver, WA 98683-9589.

artifacts reduce the accuracy obtainable with InSAR to a few centimeters (Zebker and others, 1997).

Geodetic measurements began at Augustine Volcano starting in 1986 (Power and Iwatsubo, 1998), and GPS campaign surveys were conducted repeatedly in the early 1990s and in 2000 (Pauk and others, 2001). An initial analysis did not detect any surface deformation that could be attributed to magmatic activity for the period from 1988 to 2000 (Pauk and others, 2001). The campaign GPS data were reprocessed in late 2005 (J. Freymueller, written commun., December 14, 2005). Results indicated that a shallow source (depth less than a few kilometers) beneath the volcano's summit might have deflated at a rate of less than 5 mm/yr during 1988–2000. Five continuous GPS (CGPS) stations were established in September 2004 by the EarthScope Plate Boundary Observatory (Pauk and others, this volume), and detected shallow inflation of about 2 mm/month from June 2005 to January 2006 before the 2006 eruption (Cervelli and others, 2006).

Early results based on a limited number of InSAR images indicated subsidence of 1986 pyroclastic flows on the north flank of Augustine Volcano (Lu and others, 2003). Masterlark and others (2006) constructed a finite element model that simulated post-eruptive thermoelastic contraction of the initially hot and geometrically complex 1986 pyroclastic flow deposits. By combining a 1992–1993 InSAR image, the finite element model, and an adaptive mesh algorithm to iteratively optimize the geometry of the deposit, Masterlark and others (2006) determined an initial excess temperature for the pyroclastic flow unit of 640ºC and an average thickness of 9.3 m. Lee and others (2008) systematically processed all the available InSAR images for Augustine Volcano acquired during 1992–2005 and concluded that (1) typical summer-to-summer InSAR images maintain good coherence for only about 2 years, probably because most of the volcano is mantled by pyroclastic flows and other loose materials that are easily erodible and compactable; (2) atmospheric delay anomalies typically reached 2 to 3 cm in individual interferograms; and (3) stacking multiple InSAR images revealed no significant, centimeter-scale volcano-wide deformation during 1992–2005.

The first obstacle that prevented us from reaching millimeter-scale accuracy for InSAR measurements at Augustine Volcano is atmospheric path-delay anomalies, which are caused mainly by variation in the water vapor content of the atmosphere. Studies have shown that the apparent range change caused by atmospheric delays over Augustine (Lee and others, 2008) and other Aleutian volcanoes (Lu and others, 2007) can be as large as 10 cm. Averaging multiple InSAR images tends to reduce atmospheric noise, because water vapor patterns generally are not spatially correlated over time intervals spanned by interferograms. Nevertheless, the effectiveness of InSAR for monitoring Aleutian volcanoes has been hampered by the typical presence of large atmospheric path-delay anomalies, and theoretical accuracy of 2 to 3 mm for InSAR has not been achieved. A second factor affecting InSAR measurement at Augustine is the loss of InSAR coherence for InSAR images that span more than 2 years. This is because much of the

volcano is covered by pyroclastic flows that do not maintain good coherence for C-band InSAR measurements.

Two techniques have been proposed to conduct time-series analysis of multiple interferograms to reduce atmospheric noise: (1) persistent scatterer InSAR (PSInSAR) (Ferretti and others, 2001) and (2) small baseline subset (SBAS) InSAR (Berardino and others, 2002). For PSInSAR, a single master image is used to construct all the interferograms for time-series analysis. This approach did not yield useful results for Augustine Volcano, owing to the problem with coherence loss that was mentioned previously. Instead, we used SBAS InSAR, which utilizes several master images to form interferograms with small baselines that span relatively short time intervals (and therefore tend to maintain coherence).

For this paper, we used all suitable SAR images of Augustine Volcano that were acquired from 1992 to 2005. Our objective was to detect and measure any subtle, small-scale deformation that might have occurred during the time of our investigation. We used SAR data from two independent satellite tracks to intercompare InSAR-derived deformation measurements. In addition, we compared InSAR measurements with continuous GPS measurements for the period September 2004 to October 2005. Finally, we used a two-source model to interpret the observed deformation pattern.

# Historical Eruption of Augustine Volcano

Augustine Volcano is a 1,260-m-high and 90-km² island stratovolcano in the southwestern part of Cook Inlet, about 280 km southwest of Anchorage, Alaska (fig. 1). Augustine Island formed on Jurassic and Cretaceous sedimentary strata overlain by granitoid glacial erratics and volcanic hyaloclastites (Miller and others, 1998). Augustine Volcano is one of the youngest and most active volcanoes in Cook Inlet (Begét and Kowalik, 2006), with explosive eruptions in 1812, 1883, 1935, 1963, 1976, 1986, and most recently 2006. The most violent of these eruptions was in 1883, when a debris avalanche generated a small tsunami in Cook Inlet (Miller and others, 1998). This tsunami struck the eastern and western coasts of the southern part of Cook Inlet with 6 to 8 m waves (Begét and Kowalik, 2006). Ash clouds from the 1976 eruption were observed in eastern North America and drifted across the Atlantic Ocean (Kienle and Shaw, 1979). Most eruptions of Augustine began with an initial series of vent-clearing explosions with pyroclastic flows, surges, and lahars on the volcano flanks, followed by the extrusion of andesitic lava from the volcano's summit (Waythomas and Waitt, 1998). Proximal eruption hazards include pyroclastic flows and surges, debris avalanches, lahars, ballistics, and ash fallout. Tsunamis generated by debris avalanches can reach the Alaska mainland. Volcanic ash that can drift great distances poses a threat to airliners and to people with respiratory problems (Waythomas and Waitt, 1998).

# InSAR Analysis

## Data and Preprocessing

For our analysis, we chose SAR data that were acquired from two adjacent tracks by European Remote Sensing Satellites 1 and 2 (ERS–1 and ERS–2). From 1992 to 2005, there were 27 and 25 descending scenes acquired from tracks 229 and 501, respectively. To apply the SBAS InSAR algorithm, 25 and 27 InSAR images with perpendicular baselines of less than about 300 m were created. These were distributed in five and four small-baseline subsets as shown in figures 2*A* and 2*B*, respectively. As a result of the difference in satellite positions, SAR images between adjacent tracks cannot be combined to form interferograms. All the interferograms were obtained by using a complex multilook operation, with 2 looks in the range direction and 10 looks in the azimuth direction, resulting in a pixel dimension of about 40 m by 40 m. Topographic phase contributions in the original interferograms were removed by using the 1-arc-second Shuttle Radar Topography Mission (SRTM) digital elevation model (DEM; Farr and others, 2007).

## Introduction to the SBAS InSAR Algorithm

The SBAS InSAR algorithm was recently proposed and demonstrated by Berardino and others (2002) as a means to mitigate atmospheric artifacts and topographic errors in time-sequential interferograms, and thus to obtain time-series deformation information. The algorithm uses only interferograms with small baselines that overlap in time in order to reduce spatial decorrelation.

The phase ($\Delta\phi$) of each interferogram is defined by

$$\Delta\phi(x,r) \approx \frac{4\pi}{\lambda}\Delta d(x,r) + \frac{4\pi}{\lambda}\frac{B_\perp}{r\sin\theta}\Delta z(x,r) + \tag{1}$$
$$\Delta\phi_{atmo}(x,r) + \Delta\phi_n(x,r),$$

where $x$ and $r$ are the azimuth and slant-range pixel coordinates, $\lambda$ is the radar wavelength, $\Delta d$ is the surface displacement in the radar look direction, $B_\perp$ is the perpendicular baseline, $\theta$ is the SAR look angle, $\Delta z$ is the topographic error, $\Delta\phi_{atmo}$ is the atmospheric phase-delay artifact, and $\Delta\phi_n$ is the phase due to other noise sources (Berardino and others, 2002).
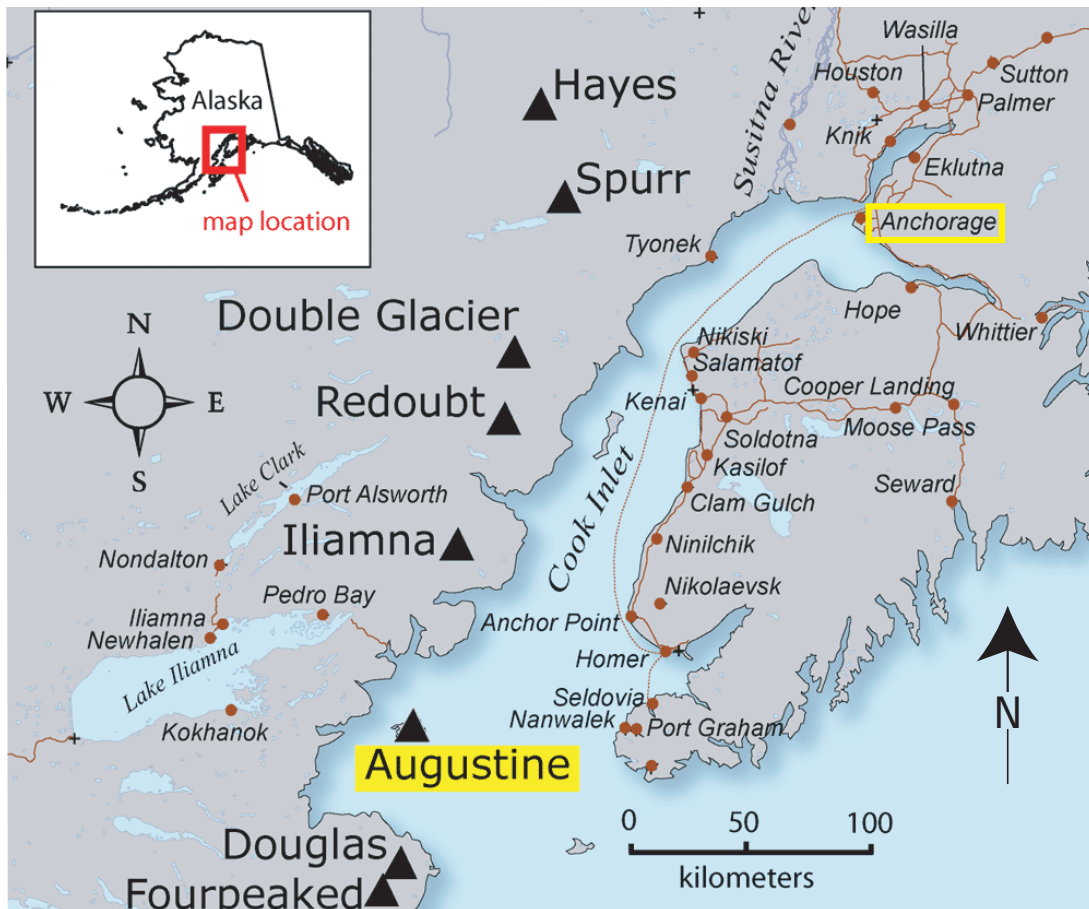


**Figure 1.**    Location of Augustine Island in the southwestern part of Cook Inlet, Alaska. Triangles, volcanoes.

To achieve deformation time-series information from multiple interferograms, the SBAS algorithm estimates the mean deformation rate and the topographic error. The atmospheric artifacts are mitigated through temporal high-pass and spatial low-pass filtering of interferograms after the mean deformation rates have been removed. Because the interferograms are not adjacently linked (there may be temporal overlap or underlap between them), SBAS InSAR uses the singular value decomposition (SVD) approach based on a minimum-norm criterion of the deformation rate to derive time-series deformation measurements.

Although this algorithm is very effective for measuring time-series deformation, the suppression of errors caused by temporal decorrelation and other noise effects is not properly addressed. Linear deformation rates estimated by using interferograms having unwrapping errors commonly lead to misestimates of the actual deformation history. Estimates of atmospheric artifacts and topographic errors based on the assumption of linear deformation rate during the periods spanned by individual interferograms can further detract from the retrieval of accurate time-series deformation measurements. Moreover, the atmospheric artifact and orbital error at the reference point (a pixel location used to reference interferogram

phase values at other pixels) have not been properly addressed, which can affect the deformation measurements.

## Refined SBAS InSAR Processing

Our refined SBAS InSAR algorithm improves estimates of time-series deformation in four respects. First, we correct phase unwrapping errors by distinguishing between high-quality (HQ) images in which no unwrapping errors could be found and low-quality (LQ) ones where phase jumps due to unwrapping errors are obvious. Second, we refine estimates of atmospheric artifacts, topographic errors, and time-series deformation measurements through an iteration procedure. Third, we further mitigate the temporal noise by the finite difference smoothing approach (Schmidt and Burgmann, 2003). Finally, we implement procedures to correct any possible phase bias at the reference point due to orbital and atmospheric phase artifacts. Specifically, the reference phase correction is based on the assumption that the mean of the unwrapped residual interferogram is approximately zero as given by

$$
\frac{1}{N_{az} N_{rg}} \sum_{i=1}^{N_{az}} \sum_{j=1}^{N_{rg}} \left[ \frac{4\pi}{\lambda} (\Delta d - \Delta \bar{d}) + \frac{4\pi}{\lambda} \frac{B_\perp}{r \sin\theta} (\Delta z - \Delta \bar{z}) + (\Delta\phi_{atmo} - \Delta\bar{\phi}_{atmo}) + \Delta\phi_n \right] \approx 0,
$$
(2)

where $N_{az}$ and $N_{rg}$ are total numbers of azimuth and range pixels; $i$ and $j$ are azimuth and range pixel coordinates; and $\Delta\bar{d}$, $\Delta\bar{z}$, and $\Delta\bar{\phi}_{atmo}$ are the estimated values of surface displacement, topographic error, and atmospheric phase delay. Equation 2 is used to correct phase values in each interferogram. The correct reference phase values should be such that the left term in equation 2 accurately represents the noise in a given interferogram (the residual phase values of the interferogram should be approximately zero after spatial averaging).

Figure 3 shows a block diagram of the refined SBAS InSAR processing algorithm. All the interferograms are classified as HQ or LQ, and the mean deformation rate ($\bar{v}$) is estimated from the HQ interferograms by using the relation

$$
\bar{v}(x,r) = \frac{\lambda}{4\pi} \frac{\sum_{k=1}^{N_{hq}} \Delta\phi_k (x,r)}{\sum_{k=1}^{N_{hq}} \Delta t_k},
$$
(3)

where $k$ is the $k$th interferogram, $N_{hq}$ is the total number of HQ interferograms and $\Delta t$ is the time difference between master and slave images. This approach is better than deriving the mean deformation rate from linear regression of the deformation rates estimated from all interferograms, because atmospheric and orbital artifacts are, to a certain degree, mitigated
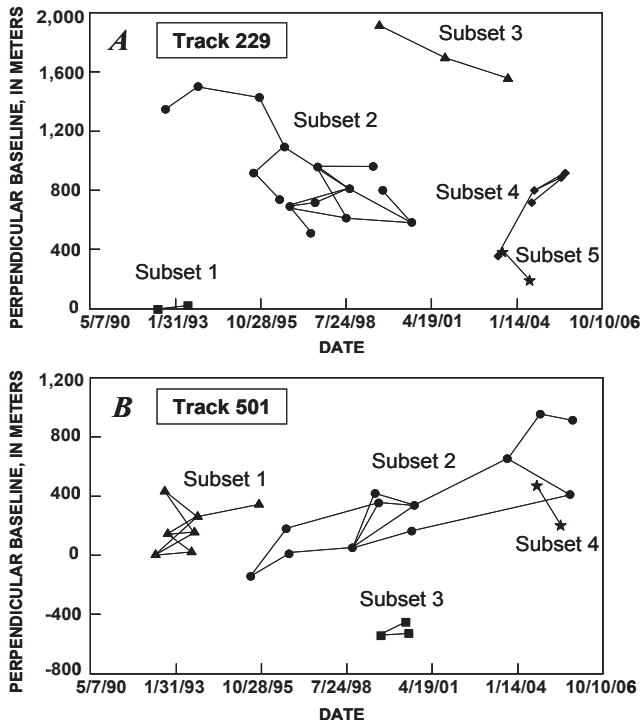


**Figure 2.** Perpendicular baselines used for small baseline subset (SBAS) interferometric synthetic aperture radar (InSAR) processing at Augustine Volcano, Alaska. *A,* Five different small baseline subsets from satellite track 229 were used for SBAS InSAR processing. *B,* Four different small baseline subsets from satellite track 501 were used for SBAS InSAR processing.
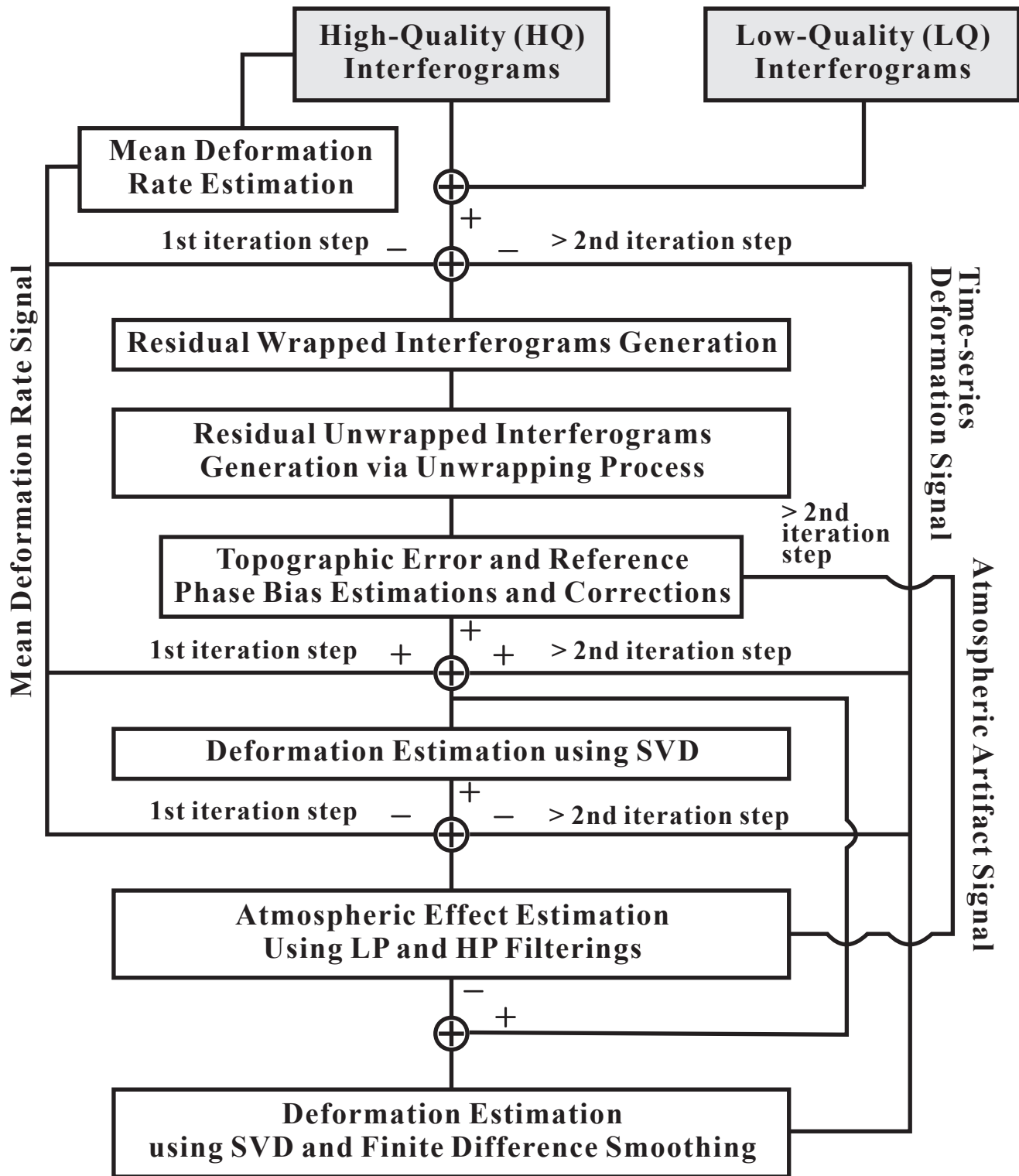
**Figure 3.** Block diagram of the refined small baseline subset (SBAS) interferometric synthetic aperture radar (InSAR) processing algorithm.

by eliminating LQ interferograms from the computation. New, wrapped residual interferograms are formed by subtracting the estimated linear deformation from each interferogram on a pixel-by-pixel basis. The residual interferograms are reunwrapped to create new unwrapped interferograms. This step essentially removes phase unwrapping errors from the LQ interferograms, because the fringe rates in the residual interferograms are much lower than those in the original interferograms.

The phase values in residual interferograms, $\phi_r$, include topographic errors that depend on the perpendicular baselines. The topographic errors are estimated from all the residual interferograms as follows:

$$\Delta z(x,r) = \frac{\lambda}{4\pi} r \sin\theta \frac{\sum_{k=1}^{N_i} \left(\Delta\phi_r\right)_k (x,r)}{\sum_{k=1}^{N_i} \left(B_\perp\right)_k} \quad , \qquad (4)$$

where $N_i$ is the total number of interferograms. The residual interferograms after removing the topographic errors are defined by

$$\left(\Delta\phi_{rt}\right)_k (i,j) = \left(\Delta\phi_r\right)_i (i,j) - \frac{4\pi}{\lambda} \frac{\left(B_\perp\right)_k}{r\sin\theta} \Delta z(i,j)$$
$$\text{for} \quad k = 1, 2, ... N_i \quad , \qquad (5)$$

where $(\Delta\phi_{rt})k$ is the $k$ th residual interferogram corrected for topographic error, and the reference phase bias ($\phi_{ref}$) for the $k$ th interferogram is estimated from coherent pixels as follows:

$$\left(\phi_{ref}\right)_k = \frac{1}{N_{az} N_{rg}} \sum_{i=1}^{N_{az}} \sum_{j=1}^{N_{rg}} \left(\Delta\phi_{rt}\right)_k (i,j)$$
$$\text{for} \quad k = 1, 2, ... N_i . \qquad (6)$$

Next, the topography-corrected interferogram phase, $\Delta\phi_{rt}$ in equation 5, is further corrected by using the reference phase bias, $\phi_{ref}$ in equation 6. At this stage, the estimated linear deformation from equation 3 is added back to the topography-corrected interferograms, in which the reference phase bias has also been corrected by using equation 6. We call the resulting interferograms "corrected interferograms."

Our next objective is to estimate and remove atmospheric artifacts. To achieve this, we estimate the time-series deformation histories at each coherent pixel by using the SVD operation, and remove them from the corrected interferograms. The atmospheric artifacts are then removed by temporal high-pass (HP) and spatial low-pass (LP) filtering operations, because the atmospheric artifacts are spatially correlated and temporally random. After the atmospheric contributions are removed in this way, we recompute the time-series deformation by simultaneously applying the SVD approach and the

finite difference smoothing method (Schmidt and Burgmann, 2003) in order to further suppress the noise contribution. This completes the first iteration of our refined SBAS InSAR processing, and results in time-series deformation estimates at each coherent pixel.

Parameter optimization and estimation in the above implementation of SBAS InSAR processing are based on the assumption of the linear deformation (equation 3). To get beyond the assumption of linearity, all processing steps are reapplied to the interferograms by using the estimated time-series deformation from the first SBAS InSAR iteration instead of the linear deformation estimated from equation 3. Our second iteration of SBAS InSAR processing corrects the topographic error, the reference phase bias, and the atmospheric artifact. Furthermore, the reference phase correction in equation 6 is refined by taking into account the estimated atmospheric artifact phase from the first iteration:

$$\left(\phi_{ref}\right)_k = \frac{1}{N_{az} N_{rg}} \sum_{i=1}^{N_{az}} \sum_{j=1}^{N_{rg}}$$
$$\left[\left(\Delta\phi_{rt}\right)_k (i,j) - \left(\Delta\overline{\phi}_{atmo}\right)_k (i,j)\right]$$
$$\text{for} \quad k = 1, 2, ... N_i . \qquad (7)$$

# Refined SBAS InSAR Applied to Augustine Volcano

We investigated surface deformation of Augustine Volcano from 1992 to 2005 using a refined multiple-interferogram processing procedure. Our SBAS InSAR processing improves the original SBAS InSAR algorithm in the following aspects:

1. We divide all InSAR interferograms into HQ and LQ interferograms, and estimate the initial mean deformation rate by using the HQ interferograms only. This is critical because the topographic error, the atmospheric contribution, and the residual phase estimate largely depend on the estimated mean deformation rate. If the mean deformation rate is estimated poorly, the measured time-series deformation will be distorted. For this reason, the initial mean deformation rate is estimated by using only high-quality interferograms in which phase coherence is good and no phase unwrapping error exists.

2. The mean deformation rate is calculated under the assumption that the deformation rate is constant. Any departure from this assumption (such as time-variant deformation) will introduce significant errors in estimating the atmospheric contribution and the topographic error. To overcome this drawback in the original SBAS InSAR algorithm, an iterative approach was applied to our refined SBAS InSAR algorithm. In the first step, our SBAS InSAR algorithm estimates the atmospheric

contribution and the topographic error by using the initial mean deformation rate, and then calculates the time-series deformation. In the second step, our algorithm estimates the atmospheric contribution and the topographic error by using the time-series deformation from the first iteration instead of the initial mean deformation rate. This approach efficiently separates the atmospheric contribution and the topographic error from interferograms and improves the time-series deformation measurement. The original SBAS InSAR algorithm does not include the iteration step

3. We have incorporated the finite-difference noise compression approach (Schmidt and Burgmann, 2003) into the original SBAS InSAR algorithm.
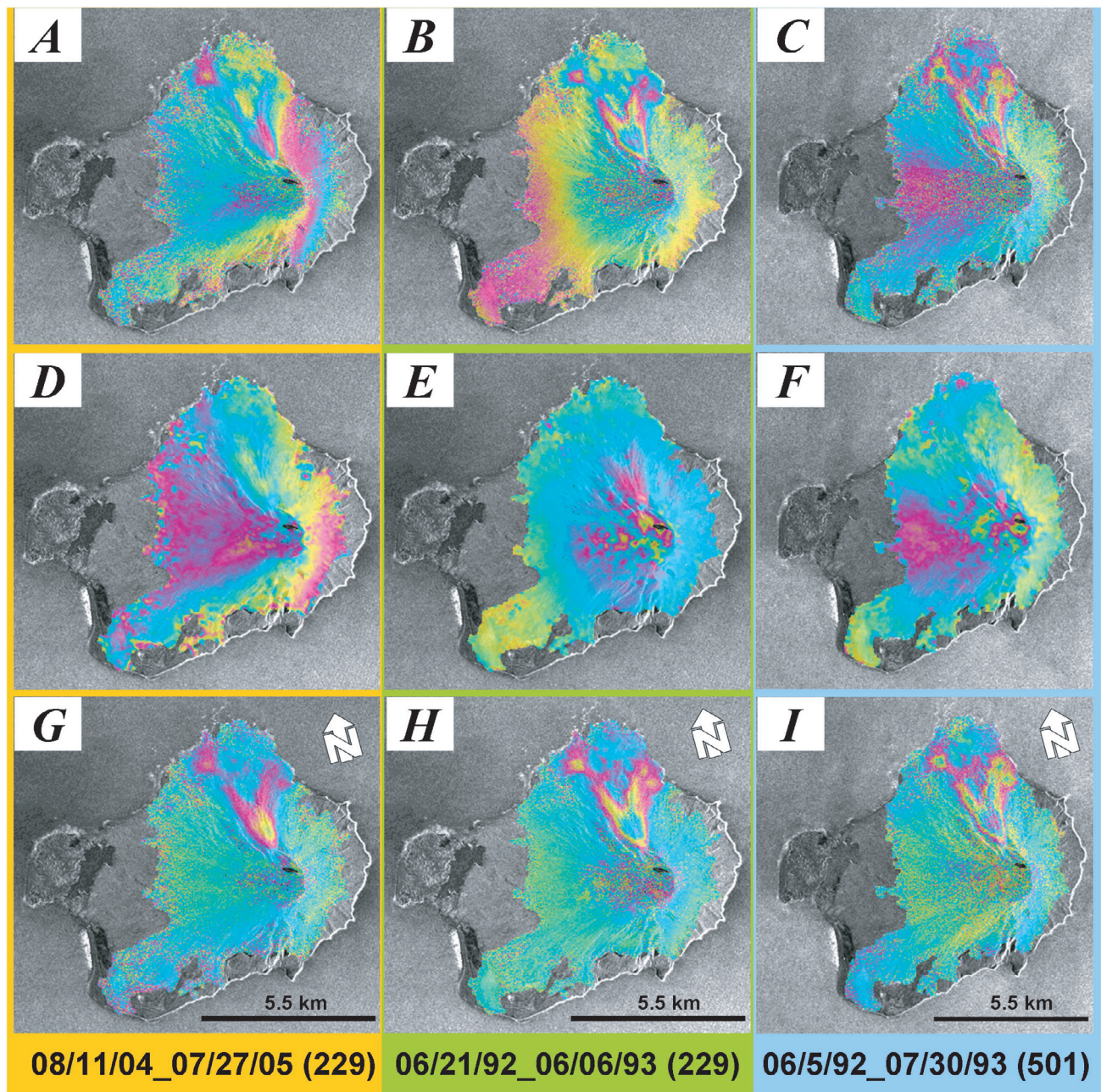


**Figure 4.** *A, B,* and *C,* Unwrapped interferograms of Augustine Volcano before small baseline subset (SBAS) interferometric synthetic aperture radar (InSAR) processing. *D, E,* and *F,* Atmospheric effects modeled using spatial low-pass filtering and temporal high-pass filtering. *G, H,* and *I,* Refined interferograms after removing atmospheric effects.

4. The reference phase correction procedure is a significant improvement in our refined SBAS InSAR algorithm. The reference phase is refined by several iteration steps. The initial reference phase correction is applied to the unwrapped residual interferograms. The correction is performed by removing the mean of the unwrapped residual interferograms and removing the bias caused by the atmospheric contribution. The initial phase correction can be slightly biased, but the bias is further corrected through iterations while the estimates of the atmospheric contribution and the topographic error are refined.

We applied the refined SBAS InSAR processing algorithm to 25 and 27 interferograms from satellite tracks 229 and 501, respectively. Among interferograms from track 229, there were 16 classified as HQ and 9 as LQ on the basis of the amount of phase unwrapping error. For track 501, there were 17 and 10 interferograms classified as HQ and LQ, respectively. A point near GPS station P2 (fig. 5) was selected as an initial reference point for SBAS InSAR processing.

Our processing procedures are briefly summarized here. During the first iteration of SBAS InSAR processing, unwrapped interferograms are corrected for the phase value at the reference point and the mean deformation rates are estimated in all coherent pixels from the HQ interferograms by using equation 3. The estimated mean deformation rates are then removed from all original wrapped interferograms (both HQ and LQ ones) to produce new wrapped residual interferograms. Then the phase unwrapping procedure is applied to the wrapped residual interferograms. We then estimate and remove topographic errors from the residual interferograms by using equation 4 and correct the reference phase bias by using equation 6. The corrected residual phase values are restored by adding back the linear deformation phase, and the initial time-series surface deformation histories are estimated from all interferograms by using the SVD approach. Spatial low-pass filtering and temporal high-pass filtering are then applied to estimate atmospheric artifacts. After the phase values due to the atmospheric contribution are removed from interferograms, the SVD approach and the finite difference smoothing method are applied simultaneously to further suppress the noise contribution. During the second iteration of SBAS InSAR processing, all processing steps are reapplied using the estimated time-series deformation histories from the first iteration. These final time-series deformation measurements are improved through iteratively refining the topographic error, the reference phase bias, and the atmospheric artifact.

Figure 4 shows three sets of interferograms, demonstrating the effectiveness of our refined SBAS InSAR algorithm in reducing atmospheric artifacts. Figures 4A–4C are three original InSAR images in which atmospheric anomalies amount to 3 to 5 cm. figures 4D–4F are primarily atmospheric artifacts modeled using spatial low-pass filtering and temporal high-pass filtering of multiple InSAR images. Figures 4G–4I are refined InSAR images in which atmospheric artifacts are mostly removed.
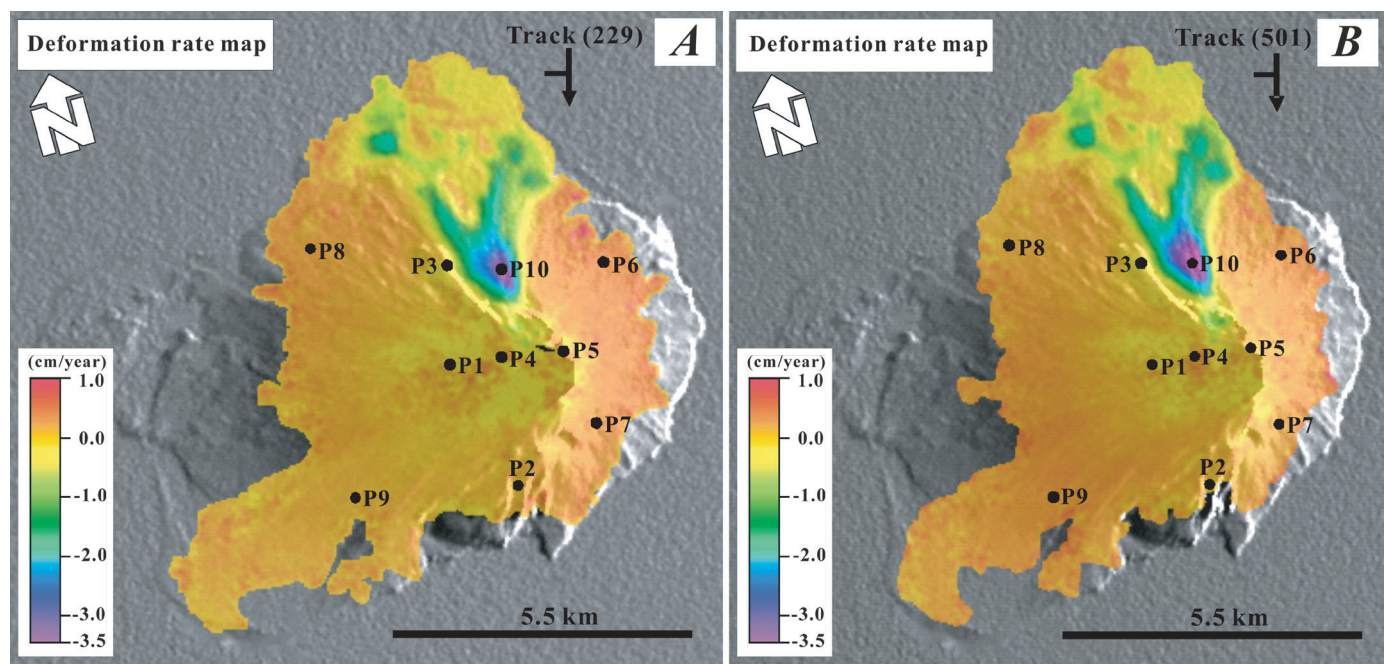


**Figure 5.**    Maps of averaged deformation rate for Augustine Volcano from the refined small baseline subset (SBAS) technique for the period 1992–2005. A, Satellite track 229. B, Satellite track 501. Results from two independent tracks show similar results. Largest displacements are associated with subsidence of 1986 pyroclastic flow deposits in upper right quadrants of the maps.

Using our SBAS InSAR processing procedure, we conducted time-series analysis for interferograms from two independent satellite tracks: 229 and 501. We do not have other time-series deformation measurements during most of the time of investigation to compare with our results, so we compared results from two independent tracks for quality assurance. Figures 5*A* and 5*B* show mean deformation rate maps for Augustine Volcano from 1992 to 2005 that were created by using the refined SBAS InSAR technique. The mean

deformation rates from the two independent tracks agree with each other well (figs. 5*A* and 5*B*). In general, we observe a wholesale uplift of Augustine Volcano, with slightly more uplift on the lower flanks.

Next, we show time-series deformation for several locations across the island. Figure 6 shows the corresponding time-series surface deformation histories at each point from tracks 229 and 501. Figures 6*A*–6*D* show surface displacement (uplift) of 4 to 6 cm for the lower flanks of Augustine
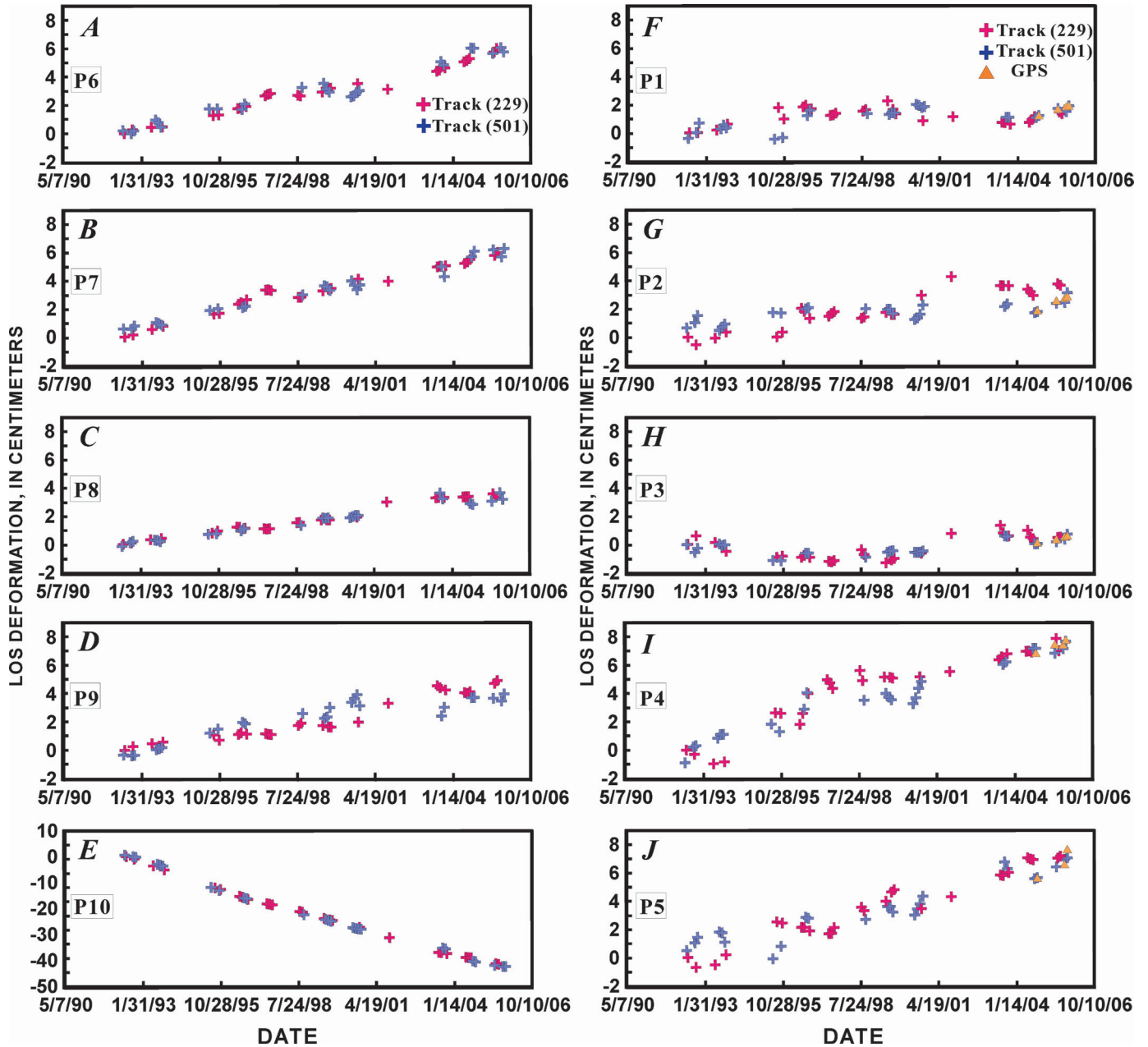


**Figure 6.**    Line-of-sight (LOS) surface-displacement time-series for selected points (see fig. 5) on Augustine Volcano for the period 1992–2005. Red and blue symbols reflect satellite tracks 229 and 501, respectively. Continuous Global Positioning System (CGPS) measurements at five locations for 2004–2005 are also shown (triangles).

Volcano during the 13 years of the investigation. Figure 6*E* shows about 40 cm of subsidence for the 1986 pyroclastic flow deposit.

A network of continuous Global Positioning System (CGPS) receivers (P1–P5) was installed on the volcano by the Plate Boundary Observatory in fall 2004 (Pauk, this volume). We used the GPS data to validate InSAR measurements for the overlapping time interval between September 2004 and October 2005. All GPS data were converted into the InSAR line-of-sight (LOS) vector. Figures 6*F*–6*J* show time-series displacement at CGPS locations, comparing SBAS InSAR results and CGPS data from September 2004 to October 2005. The CGPS displacements were projected to the LOS vector by using the InSAR imaging geometry for track 501. About 3 to 8 cm of uplift is observed at five CGPS locations (figs. 6*F*–6*J*). In general, we find that the interferometric coherence on the upper part of Augustine Volcano, where CGPS stations are located, is worse than on the lower flanks (figs. 6*A*–6*E*). This is the main reason why SBAS InSAR time-series results look noisy (figs. 6*F*–6*J*). From September 2004 to October 2005, SBAS InSAR results indicate about 5 to 15 mm uplift at the five CGPS locations. These results agree with the CGPS observations that indicate Augustine Volcano had been inflated from early summer 2005 to the time of its eruption in January 2006 (Cervelli and others, 2006; Cervelli and others, this volume).

# Deformation Modeling and Analysis

Our refined SBAS InSAR algorithm allows us to retrieve temporal surface deformation information while minimizing atmospheric artifacts, DEM errors, and phase unwrapping errors. We have processed InSAR images from two descending satellite tracks and found that the independent results indicate very similar trends, giving us confidence in our refined algorithm. CGPS observations during September 2004 to October 2005 further validate the refined SBAS InSAR processing algorithm.

Surface displacement at Augustine Volcano can be characterized as a wholesale uplift of the island by 2 to 8 cm during the 13 years of investigation. The amount of uplift of the upper flanks is slightly less than that of the lower flanks. To estimate the location of the source responsible for the observed surface displacement, we modeled the averaged deformation interferograms in figure 5 by using two point sources embedded in an elastic homogeneous half-space (Mogi, 1958). The four parameters used to describe a Mogi source are horizontal location (x, y), depth, and strength, which is related to a change in pressure, volume, or both. A nonlinear least squares

inversion approach was used to optimize the source parameters. This approach minimizes a merit function defined as the chi-squared difference between the observed and synthetic interferograms. The Levenberg-Marquardt Method (Press and others, 1992) was used to iteratively improve the trial solution until the chi-squared effectively stopped decreasing. To account for topographic effects, we adopted a simple approach proposed by Williams and Wadge (1998) in which the elevation of the reference surface varies according to the elevation of each computation point in the model.

To model the deformation by using two Mogi sources, we first masked out the subsidence associated with the 1986 pyroclastic flow deposit, which was attributed to thermoelastic contraction (Masterlark and others, 2006). Next, we used a Mogi source to model the deformation of the upper part of the volcano by masking out the deformation over the lower half. In this case, we also included three ramping phase terms ($a+bx+cy$, where $x$ and $y$ are pixel coordinates) to account for the wholesale uplift of the volcano. The best source model is located 1.7 to 3.8 km below mean sea level, with an averaged contracting volume of about 0.2 million m$^3$/yr. Using the best-fit location for this first Mogi source, we generated a modeled deformation image (fig. 7*B*) and removed it from the observed deformation image (fig. 7*A*). The resulting deformation field over the lower part of the volcano was modeled with a second Mogi source. In this case, we did not include the three ramping phase terms in order to model the long-wavelength uplift, and we fixed the horizontal location of the second source to that of the first source (the second source is located directly beneath the first). The depth of the second Mogi source is poorly constrained. The best fit was obtained with a source 7 to 12 km below mean sea level inflating at about 2 million m$^3$/yr (fig. 7*C*). Figure 7*D* shows the modeled deformation from the use of two Mogi sources, which reproduce most aspects of the observed displacement field relatively well. We recognize that our modeling is preliminary and acknowledge that many alternative models can explain the observed deformation equally well.

A preliminary two-source model that reproduces the observed displacement field at Augustine Volcano during 1992–2005 consists of a contracting source 2 to 4 km below mean sea level and an inflating source 7 to 12 km below mean sea level. The shallower source might represent a shallow magma reservoir that fed the 1976 and 2006 eruptions, and was responsible for the volcano-tectonic earthquakes at depths of 2 to 5 km below sea level that preceded the 1976 eruptions and followed the 2006 eruptions (Power and Lalla, this volume). Petrologic evidence also suggests this as a source depth for 2006 magma (Larsen and others, this volume). The deeper source could be a long-term magma storage zone beneath the volcano.
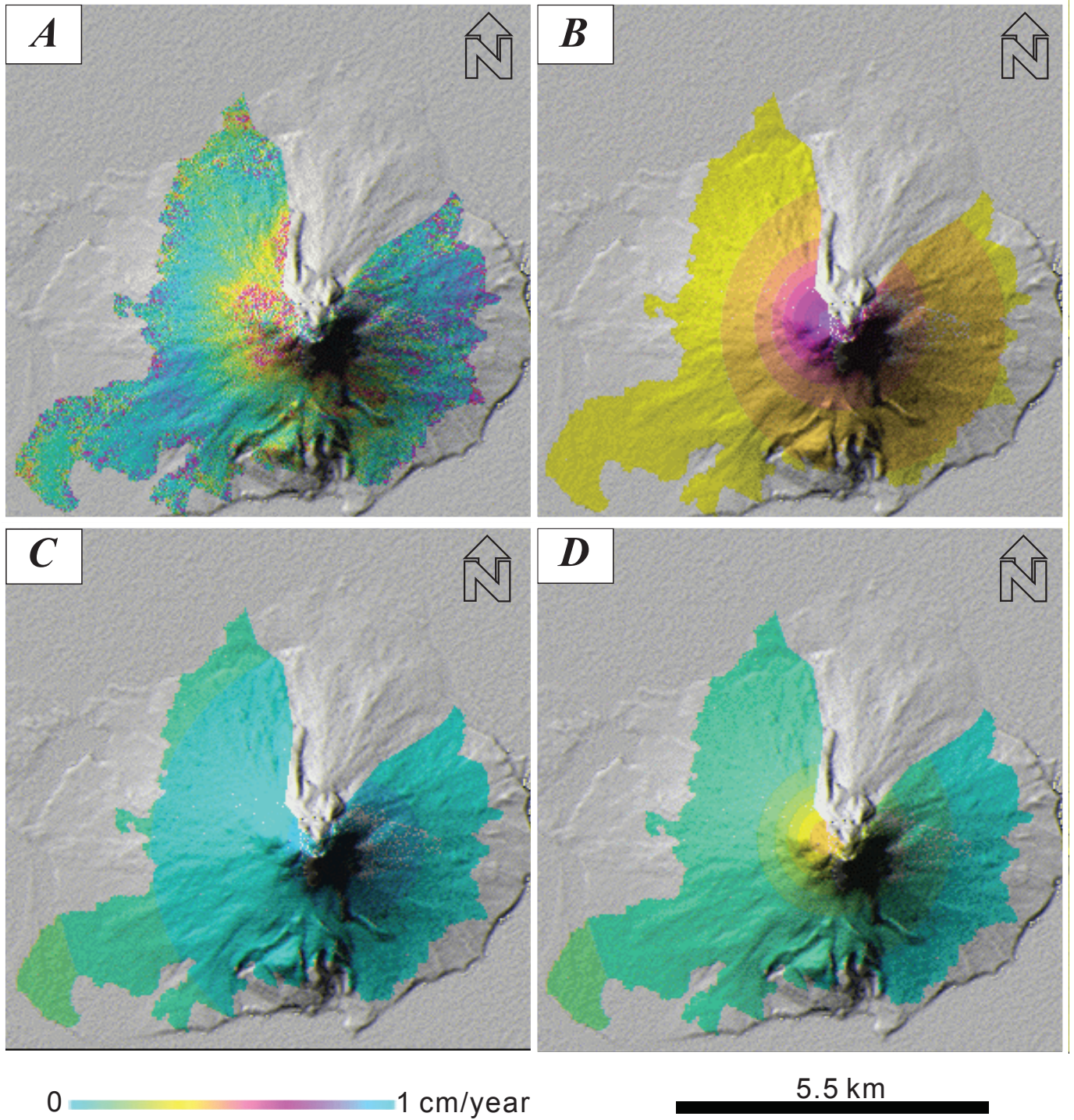
**Figure 7.**   *A,* Observed averaged deformation rate of Augustine Volcano, 1992–2005. *B,* Modeled deformation from a contracting source 3.3 km below mean sea level. *C,* Modeled deformation from an expanding source 9.6 km below mean sea level. *D,* Modeled deformation from both Mogi sources (*B* and *C*).

## Conclusions

We have developed a SBAS InSAR processing algorithm to study ground surface deformation by characterizing and removing atmospheric artifacts and DEM errors to improve surface deformation measurements through a multi-interferogram approach. The technique represents a significant advance and is particularly capable of retrieving subtle deformation over a long time interval. We applied the SBAS InSAR technique to Augustine Volcano by using SAR images from two independent datasets during 1992 and October 2005. Time-series deformation measurements from two satellite tracks agree with each other, both suggesting 2 to 8 cm uplift of the volcano during the time of investigation. The InSAR results also agree with CGPS observations at five stations that began operating in September 2004. A preliminary model consisting of a contracting Mogi source 2 to 4 km below mean level and an inflating Mogi source 7 to 12 km below mean sea level reproduces the observed displacement field reasonably well. The deeper source might represent a long-term magma storage zone beneath the volcano, and the shallower source a magma reservoir responsible for swarms of volcano-tectonic earthquakes that preceded and followed the 1976 and 2006 eruptions. Net contraction of the shallower source during a 13-year period leading up to the 2006 eruption might be a result of magma degassing or cooling. If so, both sources would seem to be long-term features of the magma plumbing system at Augustine. The shallower source, in particular, might be amenable to investigation by seismic tomography or other geophysical techniques.

## Acknowledgments

## References Cited

Begét, J.E., and Kowalik, Z., 2006, Confirmation and calibration of computer modeling of tsunamis produced by Augustine Volcano, Alaska: Science of Tsunami Hazards, v. 24, no. 4, p. 257–267.

Berardino, P., Fornaro, G., Lanari, R., and Sansoti, E., 2002, A new algorithm for surface deformation monitoring based on small baseline differential SAR interferograms: Institute of Electrical and Electronics Engineers Transactions on Geosciences and Remote Sensing, v. 40, no. 11, p. 2375–2383.

Cervelli, P., Fournier, T., Freymueller, J., and Power, J.A., 2006, Ground deformation associated with the precursory unrest and early phases of the January 2006 eruption of Augustine Volcano, Alaska: Geophysical Research Letters, v. 33, L18304, doi: 10.1029/2006GL027219.

Cervelli, P.F., Fournier, T.J., Freymueller, J.T., Power, J.A., Lisowski, M., and Pauk, B.A., 2010, Geodetic constraints on magma movement and withdrawal during the 2006 eruption of Augustine Volcano, *in* Power, J.A., Coombs, M.L., and Freymueller, J.T., eds., The 2006 eruption of Augustine Volcano, Alaska: U.S. Geological Survey Professional Paper 1769 (this volume).

Dzurisin, D., 2007, Volcano Deformation—Geodetic Monitoring Techniques: Springer Praxis Publishing Ltd., UK.

Farr, T., and 17 others, 2007, The Shuttle Radar Topography Mission: Reviews of Geophysics, 45, RG2004, doi:10.1029/2005RG000183.

Ferretti, A., Prati, C., and Rocca, F., 2001, Permanent scatterers in SAR interferometry: Institute of Electrical and Electronics Engineers Transactions on Geosciences and Remote Sensing, v. 39, p. 8–22.

Gabriel, A.K., Goldstein, R.M., and Zebker, H.A., 1989, Mapping small elevation changes over large areas—differential interferometry: Journal of Geophysical Research, v. 94, p. 9183–9191.

Kienle, J., and Shaw, G.E., 1979, Plume dynamics, thermal energy and long-distance transport of vulcanian eruption clouds from Augustine Volcano, Alaska: Journal of Volcanology and Geothermal Research, v. 6, no. 1-2, p. 139–164.

Larsen, J.F., Nye, C.J., Coombs, M.L., Tilman, M., Izbekov, P., and Cameron, C., 2010, Petrology and geochemistry of the 2006 eruption of Augustine Volcano, *in* Power, J.A., Coombs, M.L., and Freymueller, J.T., eds., The 2006 eruption of Augustine Volcano, Alaska: U.S. Geological Survey Professional Paper 1769 (this volume).

Lee, C., Lu, Z., Kwoun, O., and Won, J., 2008, Deformation of Augustine volcano, Alaska, 1992–2005, measured by ERS and ENVISAT SAR interferometry: Earth, Planets and Space, v. 60, 447–452.

Lu, Z., Wicks, C., Dzurisin, D., Power, J., Thatcher, W., and Masterlark, T., 2003, Interferometric synthetic aperture radar studies of Alaska volcanoes, Earth Observation Magazine , v. 12, no. 3, 8–18.

Lu, Z., Dzurisin, D., Wicks, C., Jr., Power, J., Kwoun, O., and Rykhus, R., 2007, Diverse deformation patterns of Aleutian volcanoes from satellite interferometric synthetic

aperture radar (InSAR), *in* Eichelberger, J.C., Gordeev, E., Izbekov, P., Kasahara, M., and Lees, J.M., eds., Volcanism and tectonics of the Kamchatka Peninsula and adjacent arcs: American Geophysical Union Geophysical Monograph 172, p. 249–261.

Masterlark, T., Lu, Z., and Rykhus, R., 2006, Thickness distribution of a cooling pyroclastic flow deposit on Augustine Volcano, Alaska—optimization using InSAR, FEMs, and an adaptive mesh algorithm: Journal of Volcanology and Geothermal Research, v. 150, p. 186–201.

Miller, T.M., McGimsey, R.G., Richter, D.H., Riehle, J.R., Nye, C.J., Yount, M.E., and Dumoulin, J.A., 1998, Catalog of the historically active volcanoes of Alaska: U.S. Geological Survey Open-File Report 98-582, 104 p.

Mogi, K., 1958, Relations between the eruptions of various volcanoes and the deformations of the ground surface around them: Bulletin of the Earthquake Research Institute, University of Tokyo, v. 36, p. 99–134.

Pauk, B.A., Jackson, M., Feaux, K., Mencin, D., and Bohnenstiehl, K., 2010, The Plate Boundary Observatory permanent global positioning system network on Augustine Volcano before and after the 2006 eruption, *in* Power, J.A., Coombs, M.L., and Freymueller, J.T., eds., The 2006 eruption of Augustine Volcano, Alaska: U.S. Geological Survey Professional Paper 1769 (this volume).

Pauk, B.A., Power, J.A., Lisowski, M., Dzurisin, D., Iwatsubo, E.Y., and Melbourne, T., 2001, Global Positioning System (GPS) survey of Augustine Volcano, Alaska, August 3–8, 2000—data processing, geodetic coordinates and comparison with prior geodetic surveys: U.S. Geological Survey Open-File Report 01-099, 20 p.

Power, J.A., and Iwatsubo, E.Y., 1998, Measurements of slope distances and zenith angles at Augustine Volcano, Alaska, 1986, 1988, and 1989: U.S. Geological Survey Open-File Report 98-0145, 17 p.

Power, J.A., and Lalla, D.J., 2010, Seismic observations of Augustine Volcano, 1970–2007, *in* Power, J.A., Coombs, M.L., and Freymueller, J.T., eds., The 2006 eruption of Augustine Volcano, Alaska: U.S. Geological Survey Professional Paper 1769 (this volume).

Press, W., Teukolsky, S., Vetterling, W., and Flannery, B., 1992, Numerical recipes in C, the art of scientific computing: Cambridge University Press, 994 p.

Schmidt, D., and Burgmann, R., 2003, Time-dependent land uplift and subsidence in the Santa Clara Valley, California, from a large interferometric synthetic aperture radar data set: Journal of Geophysical Research v. 108, no. B9, 2416, doi:10.1029/2002JB002267.

Waythomas, C.F., and Waitt, R.B., 1998, Preliminary volcano-hazard assessment for Augustine Volcano, Alaska: U.S. Geological Survey Open-File Report 98-0106, 39 p.

Williams, C.A., and Wadge, G., 1998, The effects of topography on magma reservoir deformation models—application to Mt. Etna and radar interferometry: Geophysical Research Letters., v. 25, 1549–1552.

Zebker, H.A., Amelung, F., and Jonsson, S., 2000, Remote sensing of volcano surface and internal processes using radar interferometry, *in* Mouginis-Mark, P., ed., Remote sensing of active volcanism: American Geophysical Union Monograph, v. 116, p. 179–205.

Zebker, H., Rosen, P., and Hensley, S., 1997, Atmospheric effects in interferometric synthetic aperture radar surface deformation and topographic maps: Journal of Geophysical Research, v. 102, p. 7547–7563.